AIAA 99-4163

X-33 Aerodynamic and Aeroheating Computations for Wind Tunnel and Flight Conditions

Brian R. Hollis, Richard A. Thompson, Kelly J. Murphy, Robert J. Nowak, Christopher J. Riley, William A. Wood and Stephen J. Alter
NASA Langley Research Center, Hampton, VA 23681

Ramadas K. Prabhu
Lockheed-Martin Engineering & Sciences Company Hampton, VA 23681

AIAA Atmospheric Flight Mechanics Conference
August 9-11, 1999 / Portland, OR

X–33 Aerodynamic and Aeroheating Computations for Wind Tunnel and Flight Conditions

Brian R. Hollis*†, Richard A. Thompson*, Kelly J. Murphy*,
Robert J. Nowak*†, Christopher J. Riley*‡, William A. Wood*, and Stephen J. Alter*‡
NASA Langley Research Center, Hampton, VA 23681

Ramadas K. Prabhu§
Lockheed-Martin Engineering & Sciences, Hampton, VA 23681

This report provides an overview of hypersonic Computational Fluid Dynamics research conducted at the NASA Langley Research Center to support the Phase II development of the X–33 vehicle. The X–33, which is being developed by Lockheed-Martin in partnership with NASA, is an experimental Single-Stage-to-Orbit demonstrator that is intended to validate critical technologies for a full-scale Reusable Launch Vehicle. As part of the development of the X–33, CFD codes have been used to predict the aerodynamic and aeroheating characteristics of the vehicle. Laminar and turbulent predictions were generated for the X–33 vehicle using two finite-volume, Navier-Stokes solvers. Inviscid solutions were also generated with an Euler code. Computations were performed for Mach numbers of 4.0 to 10.0 at angles-of-attack from 10 deg to 48 deg with body flap deflections of 0, 10 and 20 deg. Comparisons between predictions and wind tunnel aerodynamic and aeroheating data are presented in this paper. Aeroheating and aerodynamic predictions for flight conditions are also presented.

Nomenclature

a	speed of sound (m/s)
b	wingpsan (m)
C_A	axial force coefficient
C_N	normal force coefficient
C_m	pitching moment coefficient
H	enthalpy (J/kg)
h	heat transfer coefficient (kg/m^2-sec), $h = \dot{q}/(H_{aw} - H_w)$
h_{FR}	Fay-Riddell heating coefficient (kg/m^2-sec)
L	length (m)
M	Mach number
$\dot{q}$	heat transfer rate (W/m^2)
R	nose radius (m)
Re	Reynolds number (1/m)
S	reference area (m^2)
T	temperature (K)
U	velocity (m/sec)
α	angle-of-attack (deg)
δ_{BF}	body flap deflection (deg)
Δs	wall cell height (m)
μ	viscosity (kg/m-s)
ρ	density (kg/m^3)

Introduction

The Access to Space Study[1] conducted by NASA recommended the development of a fully Reusable Launch Vehicle (RLV)[2,3,4] to provide a next-generation launch capability at greatly reduced cost. This recommendation led to the RLV/X–33 technology program, an industry-led effort in partnership with NASA.

The X–33 vehicle will be a sub-scale technology demonstrator for a full-scale, Single-Stage-to-Orbit (SSTO) RLV. It is intended to prove the feasibility of the SSTO-RLV concept through demonstration of key design and operational aspects of the vehicle. The X–33 program began with a Phase I industry competition between several aerospace companies. Lockheed-Martin was selected by NASA for award of the Phase II contract to design, develop, construct, and fly an X-33 vehicle based on its proposed lifting-body concept[5].

As part of the X–33 industry/government partnership, the NASA Langley Research Center (LaRC) was tasked to provide aerodynamic performance data, surface aeroheating distributions, and boundary-layer transition correlations to Lockheed-Martin to support Phase II aerodynamic and aeroheating design and

* Aerospace Technologist, Aerothermodynamics Branch, Aerodynamics, Aerothermodynamics and Acoustics Competency
† Member AIAA
‡ Senior Member AIAA
§ Senior Aerospace Engineer

development. In order to provide these data, a synergistic experimental/computational research program was conducted at NASA LaRC.

Early results from the LaRC X–33 research program were presented in Refs. 6 and 7. In those works, data from early Phase II aeroheating wind tunnel tests were presented and compared with laminar and turbulent predictions generated using both a Navier-Stokes solver and a boundary-layer engineering code[6]. These early results were used to formulate and support the use of a transition onset criteria for the X–33 in flight[7].

Since the above-mentioned research was reported, additional wind tunnel tests and computations have been performed to supplement the original data base with more detailed results and to accommodate design changes to the original X–33 configuration. Detailed results from recent experimental and computational aeroheating studies have been presented in papers by Horvath[8], Hollis[9], and Berry[10]. Key results of recent Phase II experimental and computational aerodynamic research and additional computational aeroheating results are presented in this reference and in the companion paper by Murphy[11].

In the present paper, aerodynamic performance predictions from an inviscid Euler code and two Navier-Stokes codes will be presented and compared with data from several hypersonic wind tunnels. Comparisons will also be presented between wind tunnel data and Navier-Stokes aeroheating predictions, and aeroheating predictions will be presented for several points along a reference flight trajectory.

X–33 Geometry

A brief history of the X–33 configuration evolution through Phase II of the program is presented in Ref. 8. The current configuration (Fig. 1) is a lifting-body delta planform with twin vertical tails, canted fins and body flaps. The body length is 19.3 m (63.2 ft) from the nose to the end of the engine module, and the span across the canted fins is 23.2 m (76.1 ft). The canted fins have a dihedral of 20-deg and a -8.58-deg incidence angle. Reference dimensions for aerodynamic coefficients are given in Table 1.

Computational and experimental results presented in this paper are based on the F-Loft, Rev-F configuration (Lockheed designation 604B002F) and the F-Loft, Rev-G configuration (Lockheed designation 604B002G). The overall dimensions given above apply to both configurations, which differ only in that the Rev-G configuration has minor modifications to the aft, upper surface of the vehicle. The Rev-F geometry was used in the wind tunnel aeroheating tests and the Rev-G geometry was used in the wind tunnel aerodynamic tests. All computations were performed on the Rev-F configuration.

Computational Methods

Numerical Algorithms

Computational predictions for comparison with wind tunnel test data were generated using the Navier-Stokes solvers GASP[12] and LAURA[13,14] and the inviscid solver FELISA[15,16]. Wind tunnel computations were performed with GASP and LAURA using a laminar, perfect-gas thermochemical model, and with FELISA using an inviscid, perfect-gas model. Turbulent wind tunnel computations also were performed using the GASP code. Additional wind tunnel cases were computed with a CF_4 thermochemical model using LAURA and FELISA. Trajectory cases were computed with GASP and LAURA using reacting gas thermochemical models and radiative equilibrium wall temperatures.

The GASP (General Aerodynamic Simulation Program) code[12] is a three-dimensional, finite-volume, Navier-Stokes solver which incorporates numerous flux formulations, total-variation-diminishing limiters, thermochemical models, turbulence models, and time-integration methods. As discussed in Ref. 9, a third-order, upwind-biased, min-mod limited scheme with a Roe[17] flux formulation in the body-normal direction and a Van Leer[18] formulation in the other two directions, was identified as the best set of options for generating accurate aeroheating predictions. For the wind tunnel cases discussed in this paper, the perfect-gas air model was used for the wind tunnel test cases, and an equilibrium air model was used for the flight cases. The Jacobi scheme was used for time-integration. Full viscous terms were retained for all three directions and modeled with second-order central differences. Turbulent computations were performed using the Baldwin-Lomax algebraic turbulence model with the flow treated as fully turbulent from the nose of the vehicle. For the turbulent computations, the GASP code was modified to incorporate Gupta's[19] pressure gradient and compressibility corrections to the Baldwin-Lomax model.

The LAURA (Langley Aerothermodynamic Upwind Relaxation Algorithm) code[13,14] is a three-dimensional Navier-Stokes solver based on a point-implicit relaxation scheme and Roe[17] averaging with Yee's[20] Symmetric Total Variation Diminishing limiter for inviscid fluxes. The code includes perfect-gas, equilibrium, and non-equilibrium air models and a CF_4 thermochemical model. The perfect-gas air and CF_4 models were used for the wind tunnel cases, and the non-equilibrium air model was used for the flight cases.

The FELISA[15,16] software package consists of

a set of codes used for the generation of unstructured, three-dimensional, tetrahedral grids and the solution of the steady, three-dimensional Euler equations on those grids. FELISA includes solvers for both transonic and hypersonic flows and thermochemical models for air (perfect-gas and equilibrium) and CF_4. For the cases discussed in this report, the hypersonic solver was used with the perfect-gas air and CF_4 thermochemical models. The FELISA volume grid generation software is discussed in Ref. 15, and the hypersonic solver is discussed in Ref. 16. Further details of the FELISA X–33 computations are presented in Ref. 21

Grid Generation and Adaption

The GASP and LAURA Navier-Stokes flow field computations were performed on a single-block, half-body, structured grid[22] (Fig. 2). To lessen the computational requirements, the engine-module and wake were not included in this grid, and a fake-wake, solid-body representation was employed for the regions between the canted fins and the ends of the body flaps as well as between the body flaps. Note that this fake-wake surface was not included when integrating surface pressure loads to determine aerodynamic coefficients. The baseline grid, which was used for all LAURA computations, had (254 x 181 x 65) points in the longitudinal, circumferential, and normal directions, respectively. The number of grid points was decreased for the GASP computations to (127 x 181 x 65). The lower density of the GASP grid was shown to be sufficient for aeroheating computations in Ref. 9. Additionally, a series of parametric M-α computations was performed with GASP on a (65 x 91 x 33) point grid to investigate aerodynamic trends.

A GASP computation was also performed on a full-wake grid which included the engine module to determine if the fake-wake approximation had any significant effects on the computed aerodynamic parameters. This full-wake grid had 15 blocks with a total of 2.7 million grid points.

Wind tunnel computations were performed on 0.7% and 1.32% scale grids to match the sizes of the aerodynamic and aeroheating test models, respectively. Flight computations were performed on a full-scale grid.

For each angle-of-attack case, grid adaption was performed to align the outer domain of the grid with the bow shock and to cluster grid points within the wall boundary layer. Typically, the outer boundary was adjusted so that the shock was located at approximately 80% of the normal distance between the wall and outer grid boundary. Approximately 50% of the normal grid points were clustered within the wall boundary layer, and the wall cell Reynolds number ($Re_w = \rho a \Delta s / \mu)_w$ was set in the range of 10 to 20. The scheme employed to perform these manipulations is based on Ref. 14. When necessary, additional grid quality refinement and smoothing were performed using the Volume Grid Manipulation code[23].

The FELISA inviscid computations were performed on unstructured tetrahedral volume grids generated with the FELISA software package. Because the inviscid code is not capable of simulating separated flow regions, the wake of the vehicle was not included in the grid, and a fake-wake extension was employed as was done with the structured grid. Separate grids were generated for each of the different sets of FELISA wind tunnel computations. The number of tetrahedrons in the grids varied from 6.5 million to 7.9 million.

Experiment Background

The experimental aerodynamic tests which complement this study are presented in detail in Ref. 11, and the aeroheating tests are presented in Refs. 8 and 10. The goal of these tests was to define the aerodynamic and aeroheating environment of the X–33 vehicle. The aerodynamic data reported in the present work were acquired in the LaRC 20-Inch Mach 6 Air Tunnel, 31-Inch Mach 10 Air Tunnel, 20-Inch Mach 6 CF_4 Tunnel, and the Unitary Plan Wind Tunnel (UPWT), and the aeroheating data were obtained in the 20-Inch Mach 6 Air Tunnel. Size and performance information for the first three facilities can be found in Ref. 24, and the UPWT is described in Ref. 25.

Aerodynamic testing of the F-Loft, Rev-G (604B0002G) configuration was conducted with a 0.7% scale metallic force-and-moment model. Data were obtained for angles-of-attack of -4 deg to 48 deg with body flap deflections of -15 deg to +30 deg. Test Mach numbers in the various facilities ranged from 4.63 to 10, with Reynolds number from 1.6×10^5/m to 2.5×10^7/m (0.05×10^6/ft to 7.5×10^6/ft). A complete discussion of test parametrics is presented in Ref. 11. A limited uncertainty analysis is presented in that reference, in which an uncertainty corresponding to ±0.5% of the full-scale range of the force-and-moment balance is applied to all aerodynamic data.

Aeroheating testing of the F-Loft, Rev-F (64B0002F) configuration was conducted in the Langley 20-Inch Mach 6 Air Tunnel across a range of Reynolds numbers from 3.3×10^6/m to 2.5×10^7/m (1.0×10^6/ft to 7.5×10^6/ft) at angles-of-attack from 0 to 40 deg with body flap deflections of 0, 10, and 20 deg. Aeroheating data were obtained in these tests on 1.32% scale, phosphor-coated, ceramic models using the two-color, relative intensity, phosphor thermography technique[26]. The aeroheating data were then reduced and analyzed using the IHEAT code[26].

As discussed in Ref. 26, the accuracy of the phosphor technique is dependent on the temperature rise on the surface of the test model. For the windward side heating measurements presented in this report, the accuracy of the phosphor system is estimated to be ±8%, and the overall experimental uncertainty of the heating data due to all factors is estimated to be ±15%.

Computations for Wind Tunnel Cases and Comparisons with Experimental Data

Results from the computations for wind tunnel conditions are presented in this section and compared with experimental data. Comparisons for the vehicle's aerodynamics are presented in terms of the normal force (C_N) and axial force coefficients (C_A) and the pitching moment coefficient (C_m). Aeroheating comparisons are presented in terms of the ratio of heat-transfer coefficients, h/h_{FR}. The quantity h_{FR} is a reference heat-transfer coefficient, where: the wall heating rate, $\dot{q}$, is based on Fay-Riddell[27] theory for a hemisphere of the same radius as the nose of X–33 model (1.60 cm); the adiabatic wall enthalpy, $H_{aw,}$ is assumed to be equal to the total tunnel enthalpy, $H_{T,2}$; and the wall enthalpy is computed at an ambient (300 K) wall temperature.

Freestream and Boundary Conditions

Wind tunnel test case computations were performed for the operating conditions of the NASA Langley 20-Inch Mach 6 Air Tunnel, 31-Inch Mach 10 Air Tunnel, 20-Inch Mach 6 CF_4 Tunnel, and Unitary Plan Wind Tunnel. Additional cases were also computed in a M-α parametric space bounded by Mach numbers of 4.0 and 10.0 and angles-of-attack of 10 deg and 50 deg. All freestream conditions are listed in Table 2. The wall boundary condition for all wind tunnel cases was set to a uniform, ambient (300 K) temperature. This approximation has no effect on the aerodynamic predictions, and is appropriate for heating computations because the duration of an aeroheating test in these facilities is so short (< 3 sec) that changes in model wall temperature can be neglected.

Aerodynamics for M-α Parametric Space Cases

In order to investigate the effects of Mach number and angle-of-attack on the aerodynamics of the X–33 vehicle (Rev-F, no flap deflections), a series of perfect-gas GASP computations was performed across a range of Mach numbers from 4.0 to 10.0 and angles-of-attack from 10 deg to 50 deg. A constant Reynolds number of 6.59×10^6/m (2.01×10^6/ft) was maintained for all computations. The freestream temperatures for the cases were determined by linear interpolation as a function of Mach number with the temperatures anchored to the nominal operating conditions of the Mach 6 Air and Mach 10 Air wind tunnels.

Results from these computations are presented in Figs. 3-8. The predictions for the force coefficients (C_A, C_N, C_L, C_D) and the lift-to-drag ratio (L/D) all show similar behavior, where the coefficient vs. angle-of-attack curves for each variable decrease with Mach number (Figs. 3-7). A trend toward Mach number independence can also be identified by the fact that the differences between the curves decrease with increasing Mach number. The pitching moment coefficient behavior differs from that of the other coefficients in that a stronger Mach number dependency is observed (Fig. 5). For angles-of-attack between 20 deg and 40 deg, a consistent trend can be observed of a stable pitching moment curve with values of C_m increasing with Mach number. However, for $\alpha > 40$ deg, a cross-over occurs, where C_m begins decreasing with Mach number. The stability of the vehicle also decreases with Mach number after the cross-over. A similar cross-over is suggested by these results for $\alpha < 20$ deg, but the computations were not performed for low enough values of angle-of-attack to confirm this trend. This cross-over trend has also been noted by Murphy[11] in comparisons between Mach 6 and Mach 10 wind tunnel data.

These M-α parametric space computations were performed on a coarser grid (65 x 91 x 33) than the other GASP computations, with the intent of identifying trends rather than producing quantitative results. However, as shown by comparisons in Table 3 with GASP computations on a finer grid (127 x 181 x 65) for the 31-Inch Mach 10 Air Tunnel cases, the accuracy of these coarser grid results is almost as good as the those on the finer grid, at least for aerodynamics. The parametric computations are within less than ±1% of the finer grid computations except the pitching moments at $\alpha = 30$ and 40 deg, where the value of the coefficient is approaching zero.

Aerodynamics for Wind Tunnel Cases

Aerodynamic predictions for each of the wind tunnel cases are presented in this section. Normal force, axial force, and pitching moment coefficients are plotted vs. angle-of-attack for each case. Curve fits to the experimental data from Ref. 11 are plotted in these figures. Uncertainty bounds on each coefficient resulting from the ±0.5% of the balance full scale load uncertainty estimate are also indicated on each plot. Where available, C_A and C_m predictions and data for body flap deflections of 10 and 20 deg are presented in addition to the 0-deg body flap cases. Body flap deflections had little effect on the normal force, so only 0-deg body flap values are shown for C_N.

LAURA and FELISA aerodynamic predictions for the 20-Inch Mach 6 CF_4 cases are presented in Figs. 9-11. Results from both codes are in close agreement with the normal force and pitching moment coefficient data. LAURA results are in close agreement with the axial force data. As the axial forces due to viscous effects are not accounted for in the inviscid FELISA computations, these predictions are significantly lower than the data.

LAURA and FELISA results for the UPWT cases are shown in Figs. 12-14. For C_N and C_m, both codes again agree with the data to within the experimental uncertainty. The inviscid FELISA C_A values are again, as expected, lower than the data, while the LAURA prediction is slightly outside of the lower uncertainty bound.

GASP, LAURA, and FELISA computations for the 31-Inch Mach 10 Air Tunnel cases and 20-Inch Mach 6 Air Tunnel cases are shown in Figs. 15-17 and Figs. 18-20, respectively. Note that results for 10-deg and 20-deg deflected body flaps cases are also included in these plots. The inflections in the 10 and 20-deg flap deflection pitching moment curves for both tunnels at high angles-of-attack were found to result from a bow-shock/flap-shock interaction. This interaction is discussed in more detail in the "Bow-Shock/Flap-Shock Interaction" section.

For the Mach 10 cases, the GASP, LAURA, and FELISA predictions for all variables are within the experimental uncertainty except for the FELISA C_A predictions. For the Mach 6 cases, slightly higher differences between measured and computed coefficients are observed. Normal force computations are within the experimental uncertainty, but both axial force and pitching moment computations under-predict the data. These differences between computation and experiment are relatively constant for C_A, but increase with angle-of-attack for C_m.

The reason for the differences in the Mach 6 results has not been determined, but the effects of excluding the wake from the computations were examined by running a full-wake computation. As shown in Fig. 20, the pitching moment from a GASP 15-block, full-wake computation for the Mach 6, α = 36 deg case differs only slightly from that of the LAURA fake-wake computation for the same point. This agreement would suggest that the fake-wake representation is not the cause of the pitching moment discrepancies.

As discussed by Murphy[11], the pitching moment differences do not significantly affect the stability and control performance of the X–33. At high-angles-of-attack, this difference is of the same magnitude as only a few degrees of body-flap deflection. The X–33 vehicle is designed with a +30-deg body flap deflection range, but in hypersonic, high angle-of-attack flight, the X–33 is close to being trimmed without any body-flap deflections. Thus, considerable excess control ability is available to account for any uncertainties in the pitching moment predictions or experimental data.

Aeroheating for Wind Tunnel Cases

Aeroheating computations for 20-Inch Mach 6 Air Tunnel and 31-Inch Mach 10 Air Tunnel cases are presented in this section. The GASP code was used to perform both Mach 10 and Mach 6 computations and the LAURA code was used for Mach 6 computations. Aeroheating results are presented in terms of h/h_{FR} as global windward surface heating images and windward centerline heating plots.

GASP aeroheating results for the 20-Inch Mach 6 Air Tunnel α = 20, 30, and 40-deg cases and comparisons with experimental data[8,10] are presented in Figs. 21-26. As discussed in Refs. 8 and 10, the wind tunnel data exhibited laminar behavior for freestream Reynolds numbers below 1.3×10^7/m (4.0×10^6/ft). Transitional/turbulent behavior was observed above this value, with transition beginning near the aft end of the fuselage and progressing forward with increasing Reynolds number. As shown in Figs. 21-23, the laminar centerline predictions are within the estimated experimental uncertainty (±15%) of the low Reynolds number data. For the higher Reynolds numbers, data are presented in which transition occurred both naturally (due to increasing Reynolds number) and in which transition was produced artificially with small boundary layer trips placed near the nose of the vehicle[10]. The turbulent centerline predictions are within the uncertainty of the higher Reynolds number data downstream of the trips as well as on the aft end of the fuselage where transition occurred naturally. The global agreement between measurement and prediction (Figs. 24-26) is also good. A slight over-prediction of the heating along the chines can be observed in these figures, but the differences are within the experimental uncertainty. More detailed comparisons for these Mach 6 cases can be found in Ref. 9.

LAURA windward centerline heating predictions for the 20-Inch Mach 6 Air Tunnel α = 24 and 36-deg cases are plotted against wind tunnel data in Figs. 27-28. The LAURA predictions also agree with the data to within the experimental uncertainty except at the end of the body for the α = 36 deg case where LAURA slightly over-predicts the heating.

GASP computations were also performed for the 31-Inch Mach 10 Air Tunnel at angles-of-attack of 20, 30, and 40-deg, although no aeroheating tests have

yet been conducted in that facility. Computed windward centerline heating distributions for each angle-of-attack are presented in Fig. 29, and global windward heating distributions are presented in Figs. 30-32.

Bow-Shock/Flap-Shock Interaction

Computations for the 31-Inch Mach 10 Air Tunnel and 20-Inch Mach 6 Air Tunnel cases revealed the existence of an interaction at high angles-of-attack between the bow shock and the shocks created by the flaps when deflected to 10 or 20 deg. The effects of this interaction on the flow field are illustrated by the pressure contours plotted in Fig. 33, and the effects on the surface of the flaps are shown by the heating contours in Fig. 34. As discussed in Ref. 8, the reflected expansion wave caused by the interaction creates a localized heating peak where it impinges upon the surface of the flap. Note that the heating results shown in Fig. 34 are from laminar computations; wind tunnel data suggests transitional/turbulent flow in the interaction region, which produces higher heating distributions. This interaction also affects the aerodynamics of the vehicle. The lower pressure behind the expansion wave decreases the efficiency of the flaps, which causes the pitching moment to begin increasing for higher angles-of-attack. This effect can be seen in the 10-deg and 20-deg flap deflection pitching moments plotted in Figs. 17 and 20.

Flight Aeroheating Predictions

Navier-Stokes computations were performed at selected points along the Michael 9A-8 trajectory (Fig. 35), which was current at the time this research was begun. Freestream conditions for these points are listed in Table 4. Case 1 is the peak heating point on the trajectory. Cases 2, 3, and 4 were selected because their Mach numbers and angles-of-attack are close to those of aeroheating tests in the 20-Inch Mach 6 Air Tunnel and 31-Inch Mach 10 Air Tunnel (the Mach 10 tests are still pending). Case 4 is also near the second heating maxima on the trajectory, which lies in the turbulent flight regime. For all trajectory cases, a radiative equilibrium wall boundary condition with an emissivity of 0.85 was specified.

Predictions were generated for Cases 1 and 3 using LAURA with a laminar, non-equilibrium thermochemical air model and a fully-catalytic wall boundary. GASP predictions were generated for all four points using a laminar, equilibrium air model. Given the relatively low Mach numbers for these cases, the use of the equilibrium model for the GASP computations was not expected to produce any significant errors. A fully-turbulent prediction was also generated for Case 4 with GASP using the modified Baldwin-Lomax model.

Flap deflections for flight were not available when these computations were performed, and so the flaps were omitted from the grids. The LAURA grid thus had (217 x 181 x 65) points. As a result of the grid resolution study presented in Ref. 9, it was decided that the GASP computations could be run on a coarser (64 x 91 x 65) point grid in order to generate solutions more rapidly.

Computed windward and leeward centerline temperature distributions and global windward temperatures are presented for each of the four cases in Figs. 36-43. Global and centerline comparisons between GASP and LAURA results for Cases 1 and 3 (Figs. 36-37 and 40-41) show good agreement between the two codes. The use of the equilibrium model for the GASP computations is shown to be acceptable by the close agreement observed near the nose for both cases, which is where any non-equilibrium effects would be expected. The largest differences are observed on the windward centerline toward the end of the vehicle for Case 1 (Fig. 36), where the GASP temperatures are up to approximately 10% higher than the LAURA temperatures. The LAURA computations for Case 1 also suggest a shock-interaction on the canted fins (see also Ref. 8 for experimental evidence) which is not clearly distinguishable in the GASP results. These small differences on both fins and the centerline are attributed to the lower grid resolution for the GASP computations.

For case 4, both laminar and fully-turbulent GASP results are presented in Figs. 42 and 43. The fully-turbulent computation produced windward temperatures almost 300 K higher than the laminar computation on most of the windward surface.

Summary and Conclusions

Computations have been performed using the GASP and LAURA Navier-Stokes codes and the FELISA inviscid Euler code to predict the aerodynamic and aeroheating characteristics of the X–33 Phase II vehicle. These predictions were compared with wind tunnel aerodynamic and aeroheating data obtained in supersonic and hypersonic wind tunnels. Predictions were also performed for cases representative of flight conditions.

Aerodynamic computations for each of the four wind tunnels were found to fall within the estimated experimental uncertainty of the data except for the FELISA axial force predictions and the pitching moment predictions (from all codes) at the highest angles-of-attack for the 20-Inch Mach 6 Air Tunnel Cases. The FELISA axial force discrepancies were expected and were due to the absence of viscous axial

force contributions in an inviscid solver. The pitching moment discrepancies were not resolved, but were well within the control authority of the X–33 vehicle.

GASP and LAURA laminar computations and GASP turbulent computations for the 20-Inch Mach 6 Air Tunnel aeroheating cases were found to fall within the estimated ±15% uncertainty of the wind tunnel data. GASP and LAURA aeroheating predictions along a sample trajectory were found to agree to within ±10%.

The computational results presented in this paper complement the experimental aeroheating and aerodynamic databases used in the design of the X–33 vehicle and the optimization of its trajectories. Close agreement between measurements and predictions provided a greater measure of confidence in the database. The computations also confirmed seemingly anomalous experimental results such as the bow-shock/flap-shock interaction influence on the aeroheating and aerodynamic characteristics of the vehicle and the high-angle-of-attack "cross-over" of the pitching moment. Finally, the computations provided data in regions outside the simulation range of ground-based facilities.

Acknowledgements

The authors wish to thank Tom Horvath and Scott Berry of NASA Langley for providing the aeroheating data presented in this paper.

References

1. Bekey, I., Powell, R., and Austin, R., "NASA Studies Access to Space," Aerospace America, May 1994, pp. 38-43.

2. Cook, S. A., "X–33 Reusable Launch Vehicle Structural Technologies," AIAA Paper 97-10873, Nov. 1996.

3. Freeman Jr., D. C., Talay, T. A, and Austin, R. E., "Reusable Launch Vehicle Technology Program," AIAA Paper IAF 96-V.4.01, Oct., 1996.

4. Powell, R. W., Lockwood, M. K, and Cook, S. A., "The Road from the NASA Access-to-Space Study to a Reusable Launch Vehicle," AIAA Paper IAF-98-V.4.02, Sept. 1998.

5. Baumgartner, R. I., and Elvin, J. D., "Lifting Body - An Innovative RLV Concept," AIAA Paper 95-3531, Sept. 1995.

6. Hamilton II, H. H., Weilmuenster, K. J., Berry, S. A., and Horvath, T. J., "Computational/ Experimental Aeroheating Predictions for X–33 Phase II Vehicle," AIAA Paper 98-0869, Jan. 1998.

7. Thompson, R. A., Hamilton II, H. H., Berry, S. A., and Horvath, T. J., "Hypersonic Boundary Layer Transition for X–33 Phase II Vehicle," AIAA Paper 98-0867, Jan. 1998.

8. Horvath, T. J, Berry, S. A., Hollis, B. R., Liechty, D. S., Hamilton II, H. H., Merski, N. R., "X–33 Experimental Aeroheating at Mach 6 Using Phosphor Thermography," AIAA Paper 99-3558, June 1999.

9. Hollis, B. R., Horvath, T. J., Berry, S. A., Hamilton II, H. H., and Alter, S. J., "X–33 Computational Aeroheating Predictions and Comparisons with Experimental Data," AIAA Paper 99-3559, June 1999.

10. Berry, S. A., Horvath, T. J., Hollis, B. R., Thompson, R. A., Hamilton II, H. H., "X–33 Hypersonic Boundary Layer Transition," AIAA Paper 99-3560, June 1999.

11. Murphy, K. J., Nowak, R. J., Hollis, B. R., and Thompson, R. A., "X–33 Hypersonic Aerodynamic Characteristics," AIAA 99-4162, Aug. 1999.

12. AeroSoft, "GASP Version 3, The General Aerodynamic Simulation Program, Computational Flow Analysis Software for the Scientist and Engineer, User's Manual," AeroSoft Inc., Blacksburg, VA, May 1996.

13. Gnoffo, P. A., "An Upwind-Biased, Point-Implicit Algorithm for Viscous, Compressible Perfect-Gas Flows," NASA TP 2953, Feb. 1990.

14. Cheatwood, F. M., and Gnoffo, P. A., "User's Manual for the Langley Aerothermodynamic Upwind Relaxation Algorithm (LAURA)," NASA TM 4674, April 1996.

15. Peiro, J., Peraire, J., and Morgan, K., "FELISA System Reference Manual and User's Guide," Technical Report, University College, Swansea, Wales, 1993. NASA CP-3291, May 1995.

16. Bibb, K. L., Periare, J., and Riley, C. J., "Hypersonic Flow Computation on Unstructured Meshes," AIAA Paper 97-0625, Jan. 1997.

17. Roe, P. L., "Approximate Riemann Solvers, Parameter Vectors and Difference Schemes," *Journal of Computational Physics*, Vol. 43, No. 2, 1981, pp. 357-372.

18. Van Leer, B., "Flux Vector Splitting for the Euler Equations," *Proceedings of the 8th International Conference on Numerical Methods in Fluid Dynamics*, Springer Verlag, Berlin, 1981.

19. Gupta, R. N., Lee, K. P., Zoby, E. V., Moss, J.N. And Thompson, R. A., "Hypersonic Viscous Shock-Layer Solutions over Long Slender Bodies - Part 1: High Reynolds Number Flows," *Journal of Spacecraft and Rockets*, Vol. 27, No. 2, pp. 175-184, March-April 1990.

20. Yee, H. C., "On Symmetric and Upwind TVD Schemes," NASA TM 88325, 1990.

21. Prabhu, R. K., "A Computational Study of an X–33 Configuration at Hypersonic Speeds," NASA/CR-1999-209366, July 1999.

22. Alter, S. J., "Grid Generation Techniques Utilizing

the Volume Grid Manipulator," AIAA Paper 98-3012, June 1998.
23. Alter, S. J., "The Volume Grid Manipulator (VGM): A Grid Reusability Tool," NASA CR-4772, April 1997.
24. Micol, J. R. "Hypersonic Aerodynamic/ Aerothermodynamic Testing Capabilities at Langley Research Center: Aerothermodynamic Facilities Complex," AIAA Paper 95-2107, June 1995
25. Jackson, C. M., Corlett, W. A., and Monta, W. J., "Description and Calibration of the Langley Unitary Plan Wind Tunnel," NASA TP-1905, Sept. 1981.
26. Merski, N. R., "Global Aeroheating Wind-Tunnel Measurements Using Improved Two-Color Phosphor Thermography Method," *Journal of Spacecraft and Rockets*, Vol. 36, No. 2, March-April 1999, pp. 160-170.
27. Fay, J. A. and Riddell, F. R., "Theory of Stagnation Point Heat Transfer in Dissociated Air," *Journal of Aeronautical Sciences*, Vol. 15, No. 2., 1958.

Table 1. Reference Dimensions for X–33 F-Loft, Rev-F

Dimension	Full-Scale	1.32%	0.7%
S_{ref}	149.4 m^2 (1608 ft^2)	2.60 cm^2	0.732 cm^2
L_{ref}, L	19.3 m (63.2 ft)	25.4 cm	13.5 cm
B	23.2 m (76.1 ft)	30.6 cm	16.2 cm
B_{ref}	11.2 m (36.6 ft)	14.8 cm	7.84 cm
$C.G._{ref}$	12.7 m (41.7 ft)	16.8 cm	8.89 cm
R_{ref}	1.21 m (3.97 ft)	1.60 cm	0.847 cm

Table 2. Flow Conditions for Wind Tunnel Cases

	Mach	T_∞ (K)	ρ_∞ (kg/m^3)	U_∞ (m/s)	Re_∞ (1/m)	α (deg)
20-Inch Mach 6 Air	5.99	62.1	6.28e-2	945.1	1.33e7	12,20, 24, 30, 36, 40, 48
31-Inch Mach 10 Air	9.98	48.9	1.71e-2	1414.0	6.84e6	12,20, 24, 30, 36, 40, 48
Unitary Plan Wind	4.63	65.0	7.45e-2	742.2	1.18e7	24,36,48
20-Inch Mach 6 CF_4	6.02	170	1.77e-2	849.3	1.48e6	24,36,48
M-α Parametrics	4.0	68.0	4.88e-2	660.1	6.59e6	10, 20, 30, 40
	5.0	65.0	3.81e-2	807.6	6.59e6	10, 20, 30, 40, 50
	6.0	62.0	3.10e-2	946.4	6.59e6	10, 20, 30, 40, 50
	8.0	56.0	2.20e-2	1198.4	6.59e6	10, 20, 30, 40, 50
	10.0	50.0	1.66e-2	1413.8	6.59e6	10, 20, 30, 40, 50

Table 3. Differences in Coarse and Fine Grid Aerodynamic Predictions for Mach 10 Cases

	GASP (127 x 181 x 65)	GASP (65 x 91 x 33)	% difference
C_A at $\alpha = 20$	0.1202	0.1206	+0.33
C_N at $\alpha = 20$	0.3391	0.3388	-0.09
C_m at $\alpha = 20$	0.0113	0.0114	+0.88
C_A at $\alpha = 30$	0.1192	0.1195	+0.25
C_N at $\alpha = 30$	0.6833	0.6813	-0.30
C_m at $\alpha = 30$	0.0071	0.0073	+2.82
C_A at $\alpha = 40$	0.1143	0.1144	+0.09
C_N at $\alpha = 40$	1.0541	1.0544	+0.03
C_m at $\alpha = 40$	0.0022	0.0019	-13.6

Table 4. Flow Conditions for Michael 9A-8 Trajectory Cases

	Mach	T_∞ (K)	ρ_∞ (kg/m^3)	U_∞ (m/s)	Re_∞ (1/m)	α (deg)
Case 1	8.82	265.9	7.07e-4	2887.3	1.07e5	10
Case 2	8.87	258.5	5.13e-4	2863.5	7.88e4	20
Case 3	8.89	252.1	3.87e-4	2833.5	5.97e4	30
Case 4	6.64	263.1	2.09e-3	2147.4	2.38e5	40

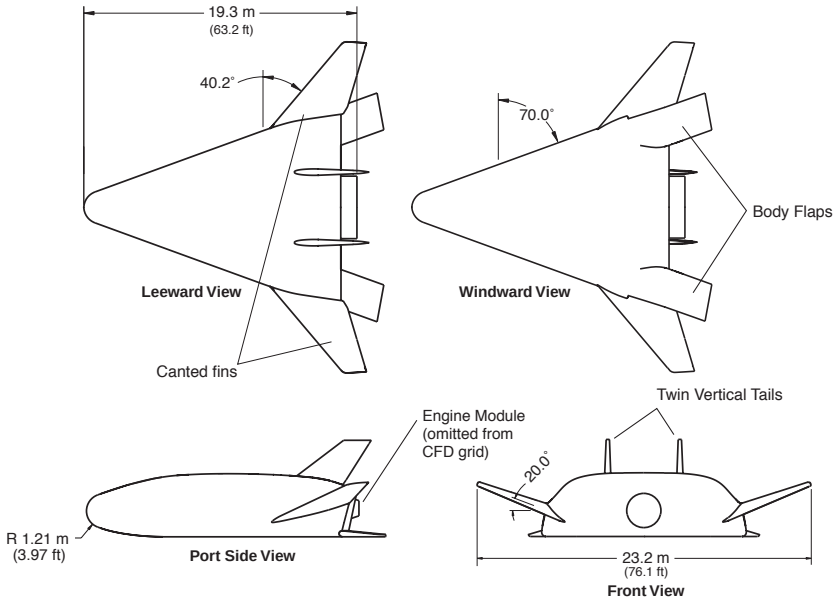

Figure 1. Sketch of Full-Scale X–33 F-Loft, Rev-F Vehicle

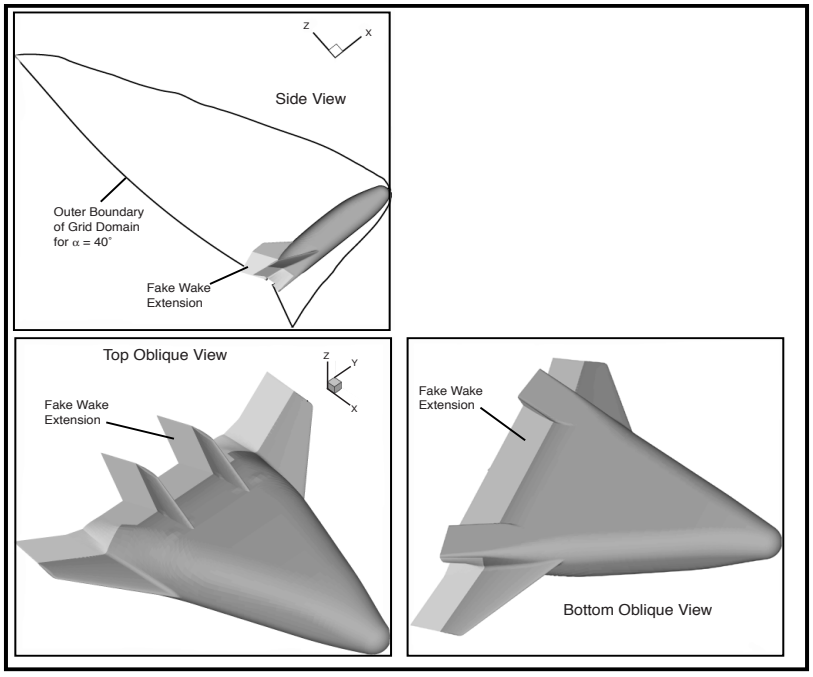

Figure 2. X–33 Computational Surface Geometry with Fake-Wake Extension

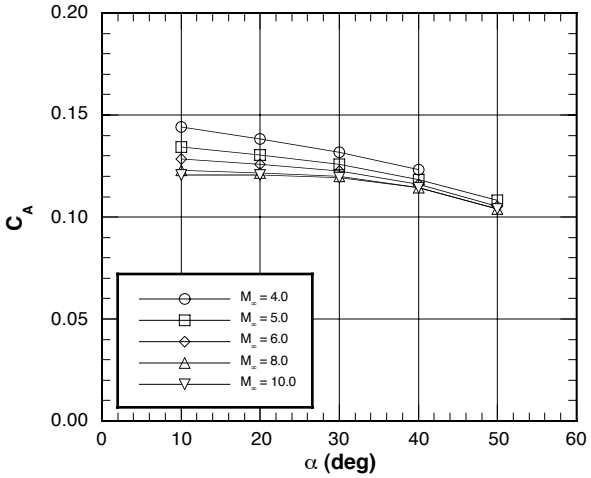

Figure 3. GASP Computations for Variation of Axial Force Coefficient with Mach Number and Angle-of-Attack

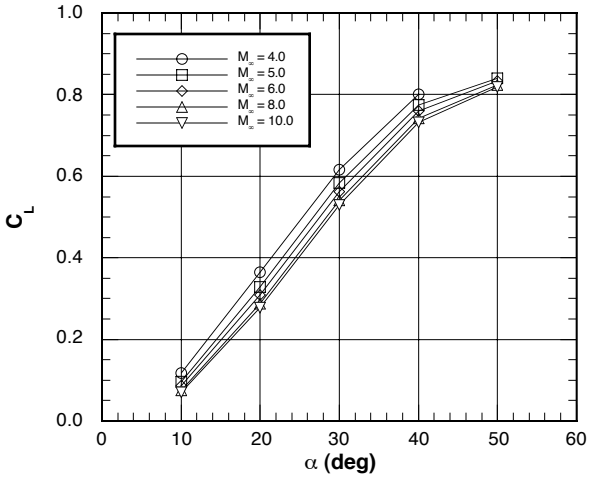

Figure 6. GASP Computations for Variation of Lift Coefficient with Mach Number and Angle-of-Attack

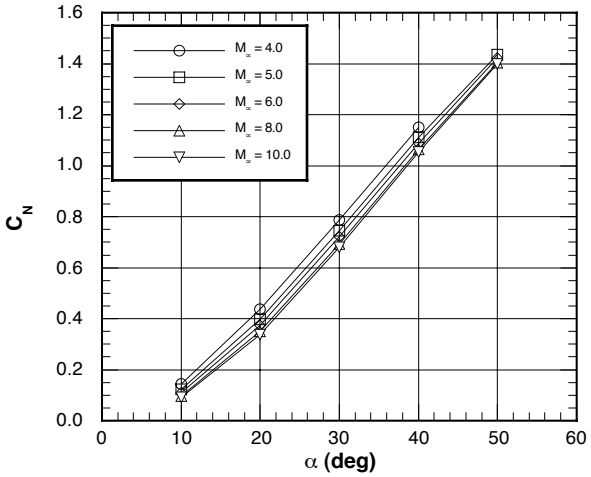

Figure 4. GASP Computations for Variation of Normal Force Coefficient with Mach Number and Angle-of-Attack

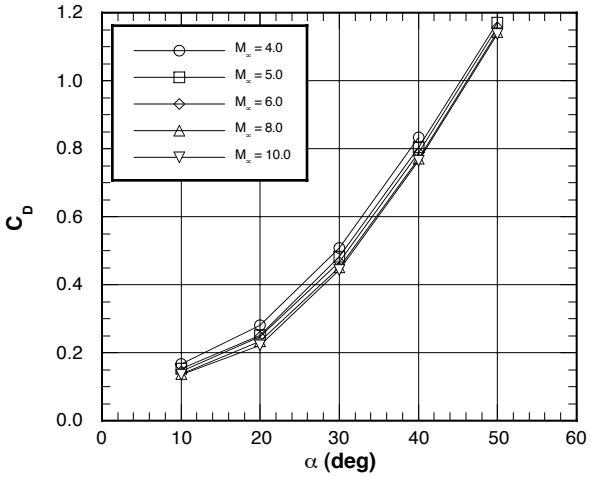

Figure 7. GASP Computations for Variation of Drag Coefficient with Mach Number and Angle-of-Attack

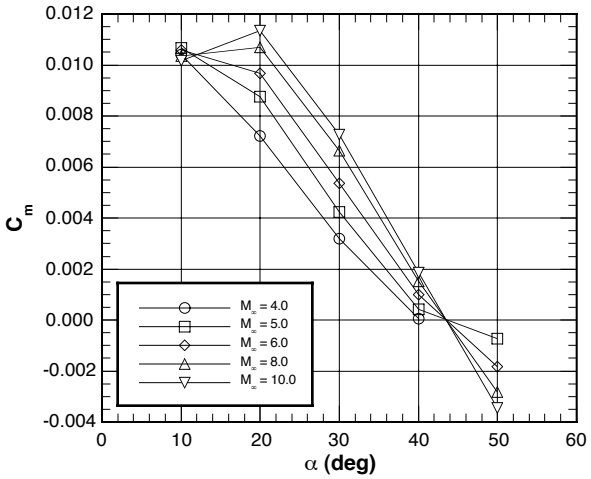

Figure 5. GASP Computations for Variation of Pitching Moment Coefficient with Mach Number and Angle-of-Attack

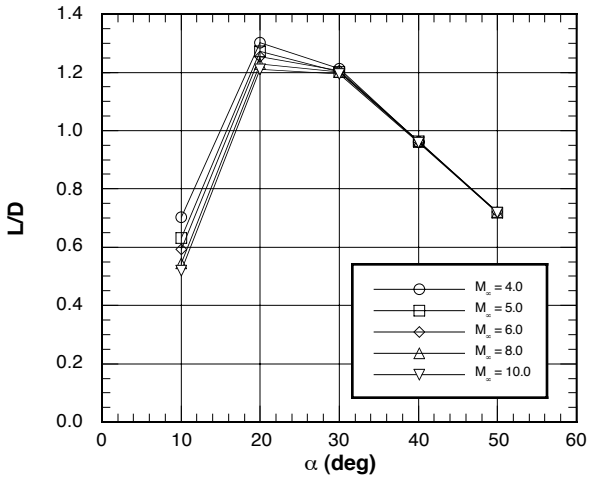

Figure 8. GASP Computations for Variation of Lift-to-Drag Ratio with Mach Number and Angle-of-Attack

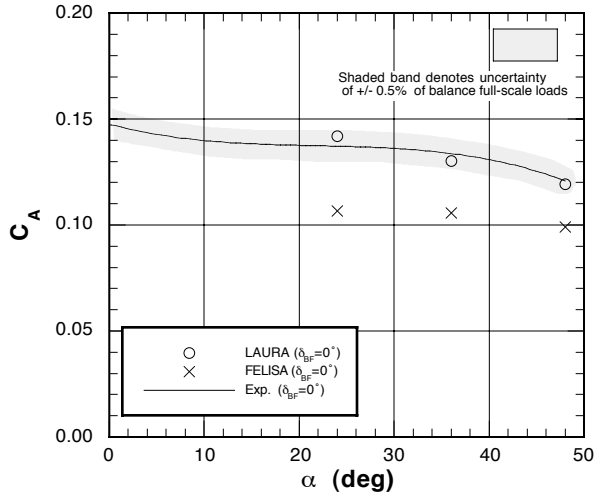

Figure 9. Comparison of Measured and Predicted Axial Force Coefficient for 20-Inch Mach 6 CF_4 Tunnel

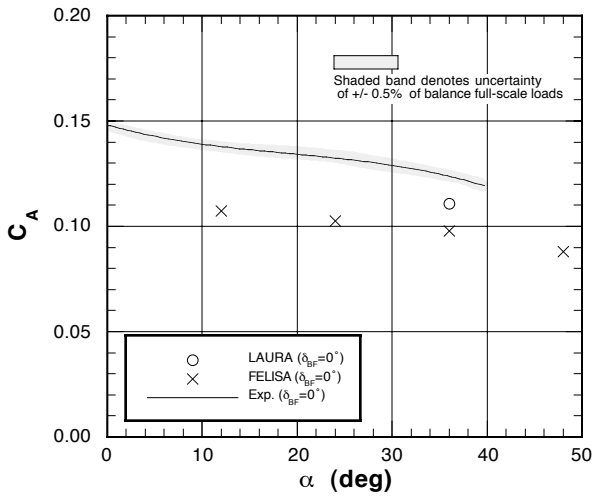

Figure 12. Comparison of Measured and Predicted Axial Force Coefficient for Unitary Plan Wind Tunnel

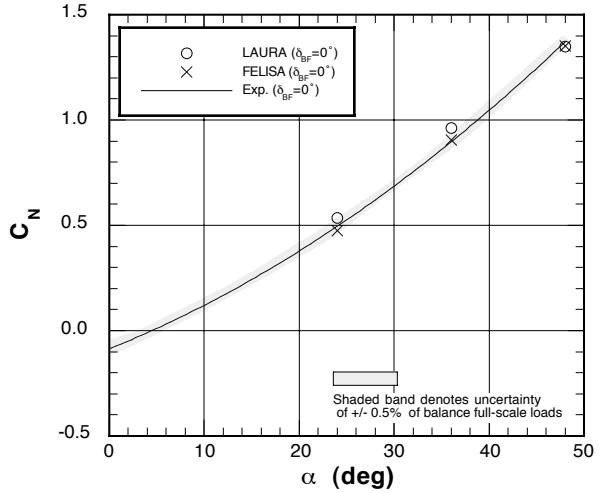

Figure 10. Comparison of Measured and Predicted Normal Force Coefficient for 20-Inch Mach 6 CF_4 Tunnel

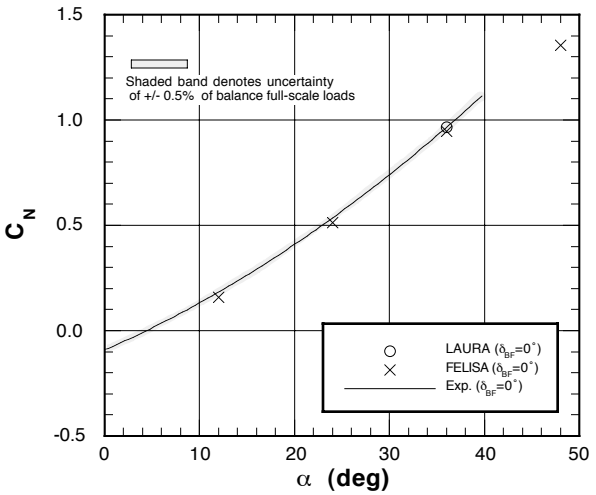

Figure 13. Comparison of Measured and Predicted Normal Force Coefficient for Unitary Plan Wind Tunnel

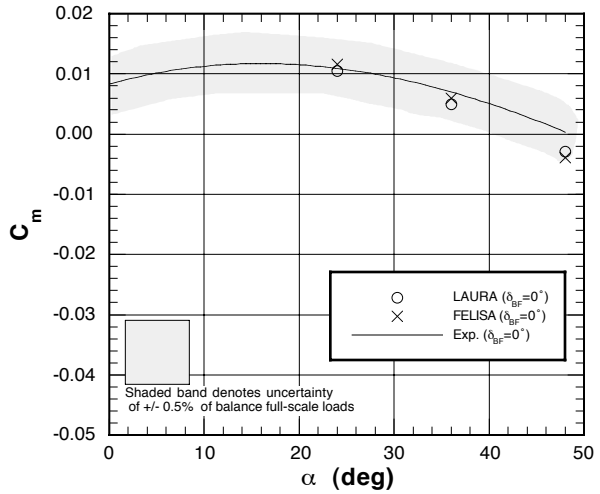

Figure 11. Comparison of Measured and Predicted Pitching Coefficient for 20-Inch Mach 6 CF_4 Tunnel

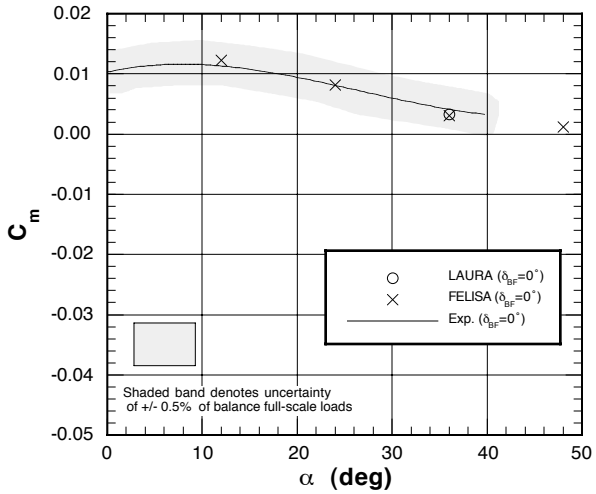

Figure 14. Comparison of Measured and Predicted Pitching Moment Coefficient for Unitary Plan Wind Tunnel

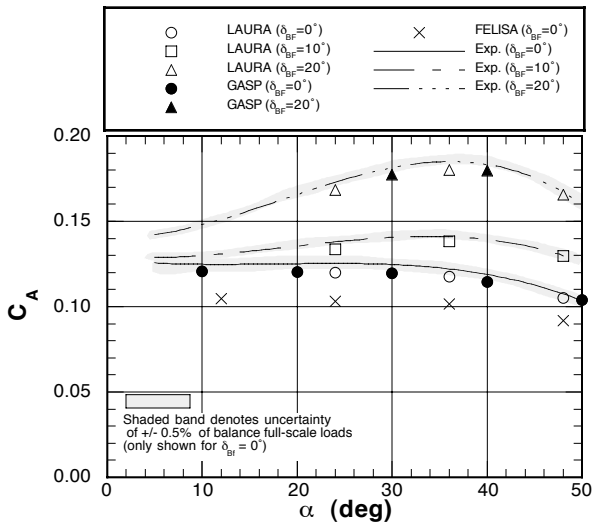

Figure 15. Comparison of Measured and Predicted Axial Force Coefficient for 31-Inch Mach 10 Air Tunnel

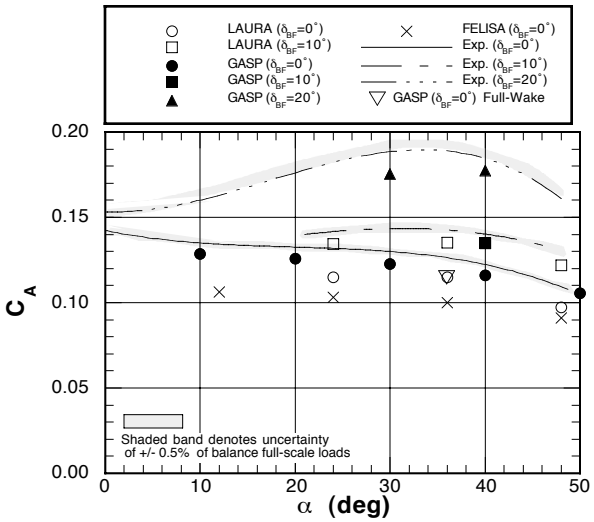

Figure 18. Comparison of Measured and Predicted Axial Force Coefficient for 20-Inch Mach 6 Air Tunnel

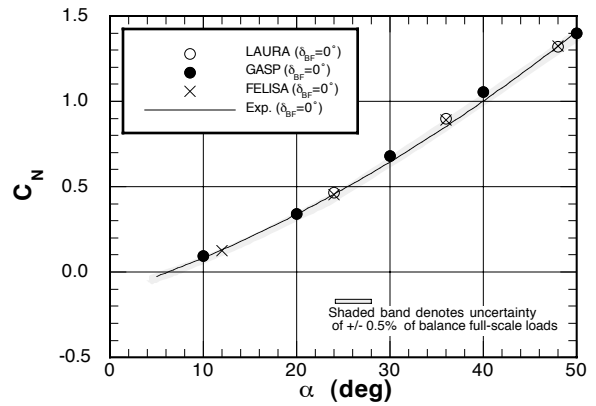

Figure 16. Comparison of Measured and Predicted Normal Force Coefficient for 31-Inch Mach 10 Air Tunnel

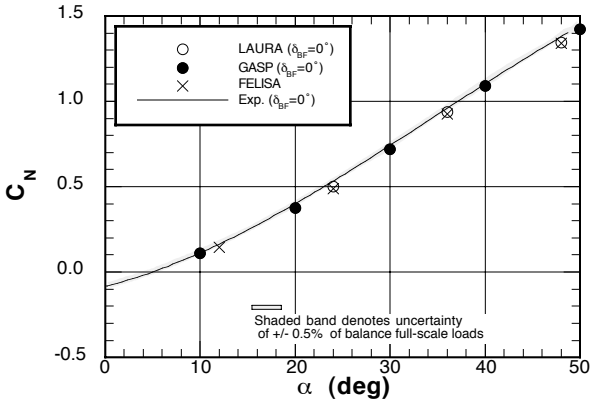

Figure 19. Comparison of Measured and Predicted Normal Force Coefficient for 20-Inch Mach 6 Air Tunnel

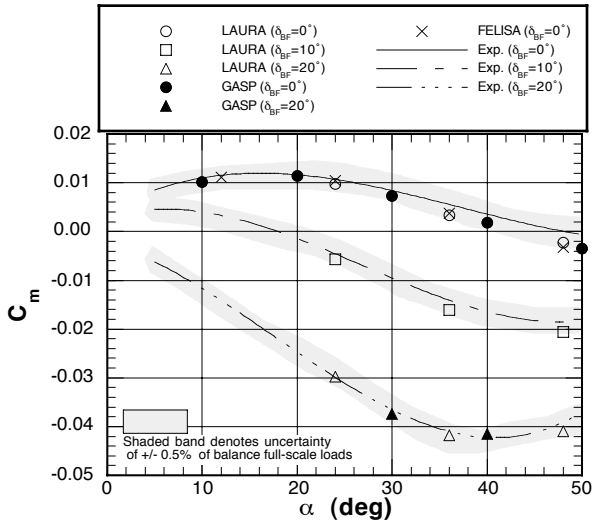

Figure 17. Comparison of Measured and Predicted Pitching Moment Coefficient for 31-Inch Mach 10 Air Tunnel

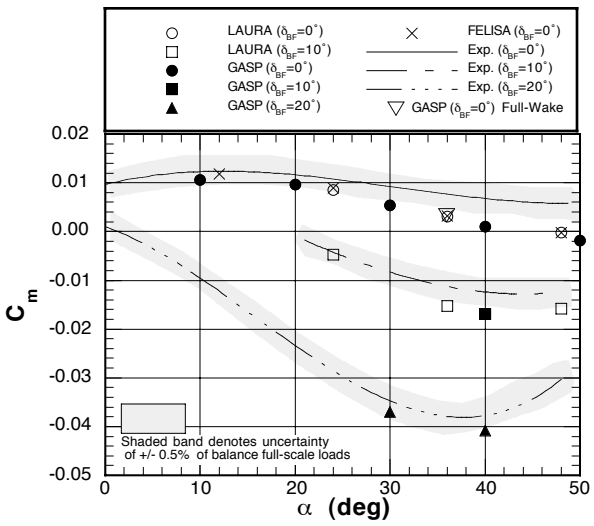

Figure 20. Comparison of Measured and Predicted Pitching Moment Coefficient for 20-Inch Mach 6 Air Tunnel

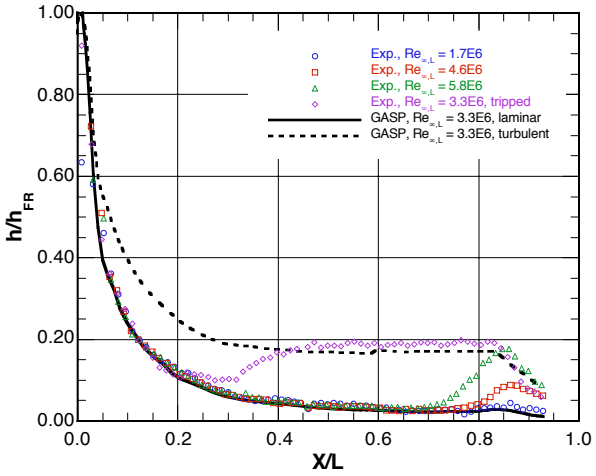

Figure 21. Windward Centerline Heating Comparison between Computations and Data for Mach 6, α = 20 deg case

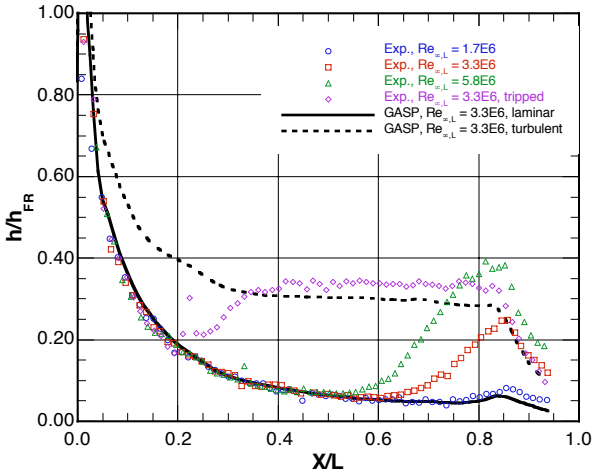

Figure 22. Windward Centerline Heating Comparison between Computations and Data for Mach 6, α = 30 deg case

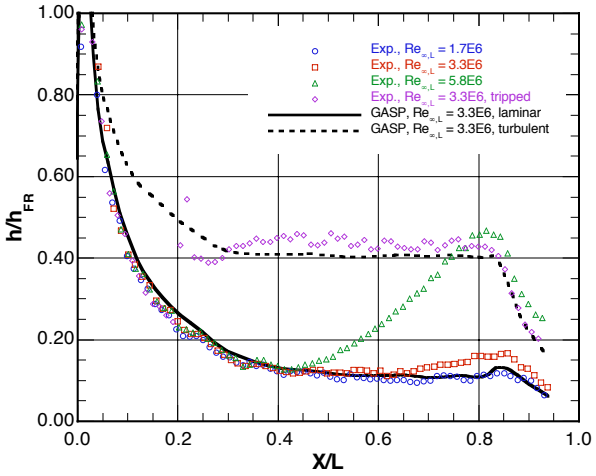

Figure 23. Windward Centerline Heating Comparison between Computations and Data for Mach 6, α = 40 deg case

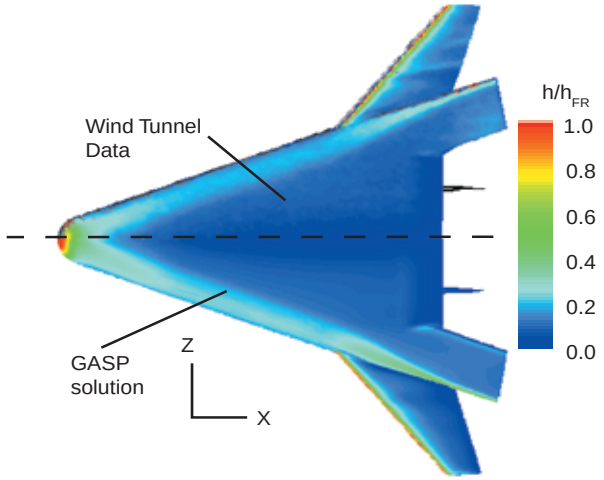

Figure 24. Windward Global Heating Comparison between Computations and Data for Mach 6, α =20 deg case

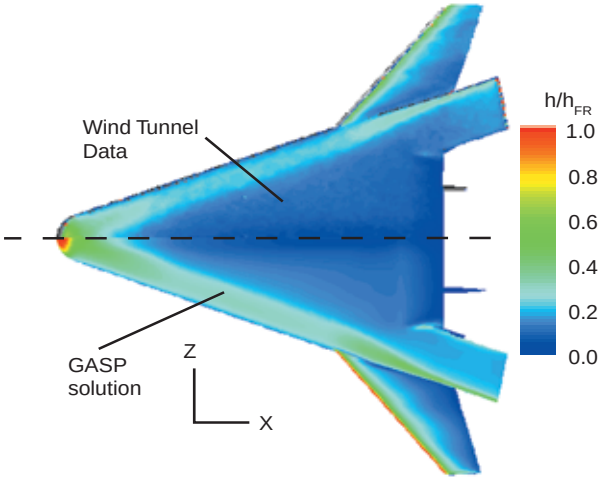

Figure 25. Windward Global Heating Comparison between Computations and Data for Mach 6, α =30 deg case

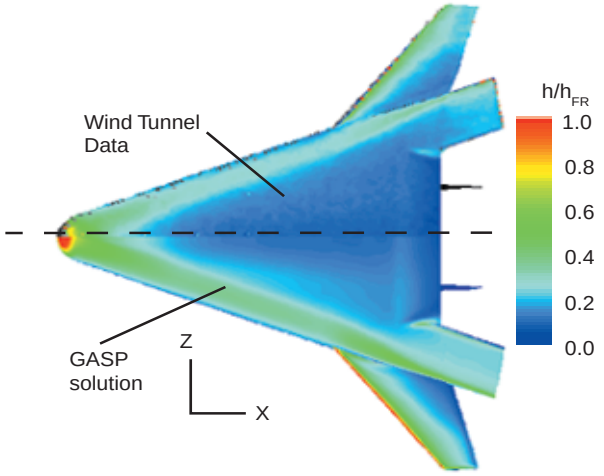

Figure 26. Windward Global Heating Comparison between Computations and Data for Mach 6, α =40 deg case

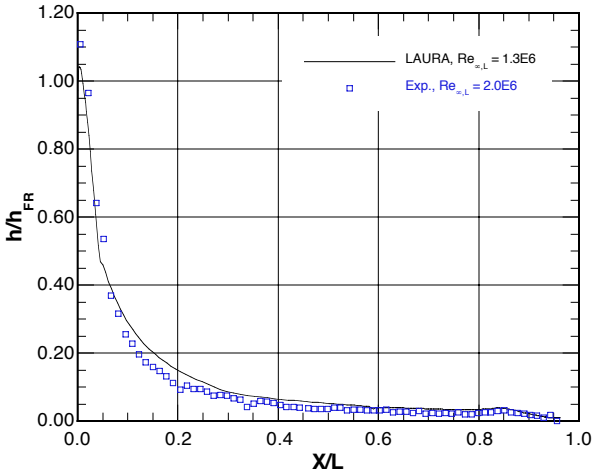

Figure 27. Windward Centerline Heating Comparison between Computations and Data for Mach 6, α = 24 deg case

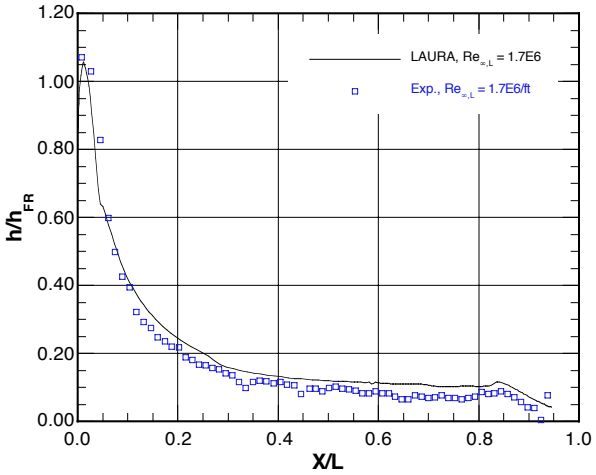

Figure 28. Windward Centerline Heating Comparison between Computations and Data for Mach 6, α = 36 deg case

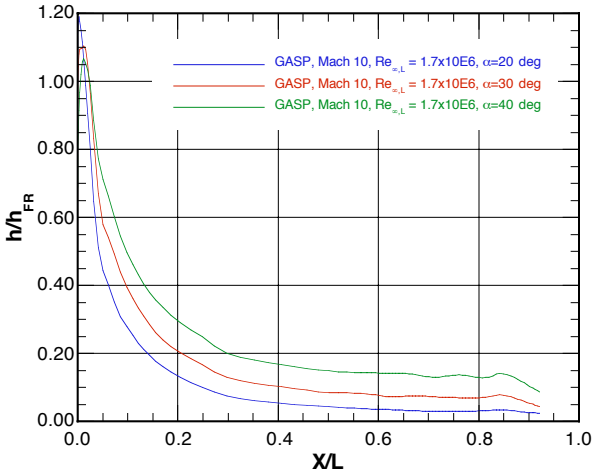

Figure 29. Windward Centerline Heating Predictions for Mach 10, α = 20, 30, 40 deg Cases

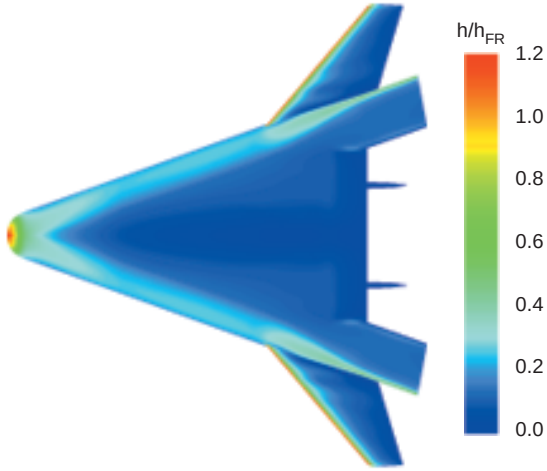

Figure 30. GASP Global Heating Computations for Mach 10, α = 20 deg Case

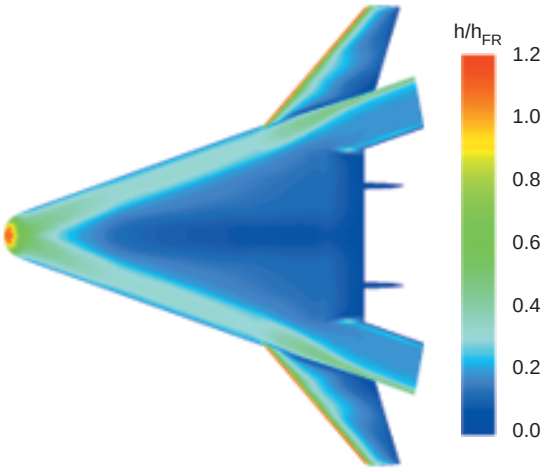

Figure 31. GASP Global Heating Computations for Mach 10, α = 30 deg Case

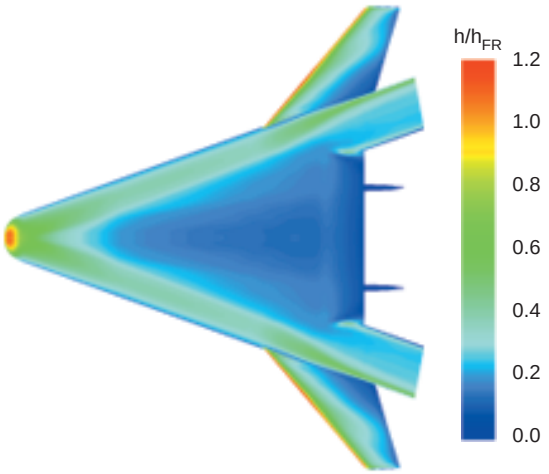

Figure 32. GASP Global Heating Computations for Mach 10, α = 40 deg Case

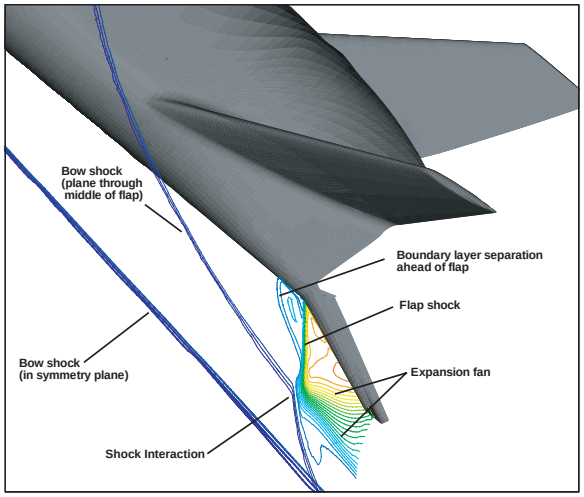

Figure 33. Pressure Contours Showing Shock-Shock Interaction for Mach 6, α = 40 deg Case

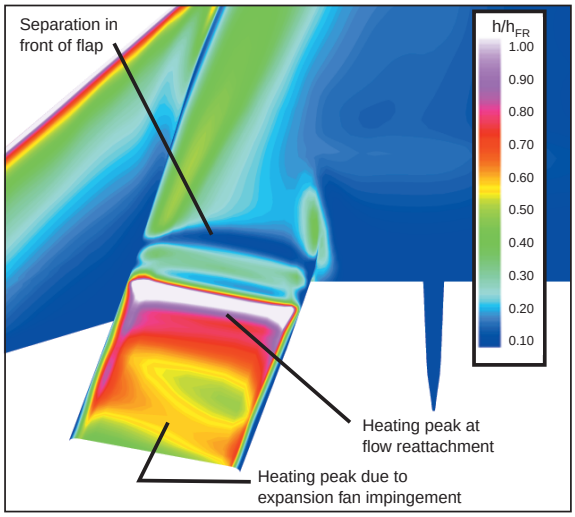

Figure 34. Heating Contours Showing Shock-Shock Interaction Effects for Mach 6, α = 40 deg Case

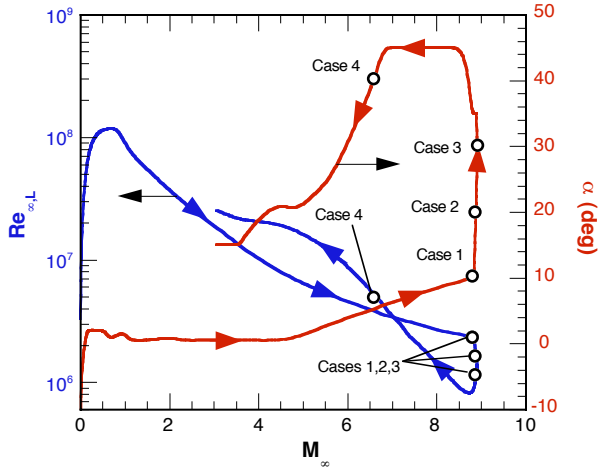

Figure 35. Points for Computations along Michael 9A-8 Tracjectory

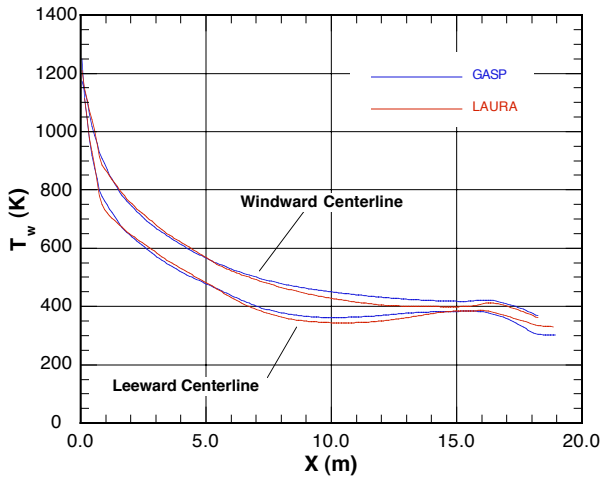

Figure 36. Computed Centerline Temperatures for Case 1

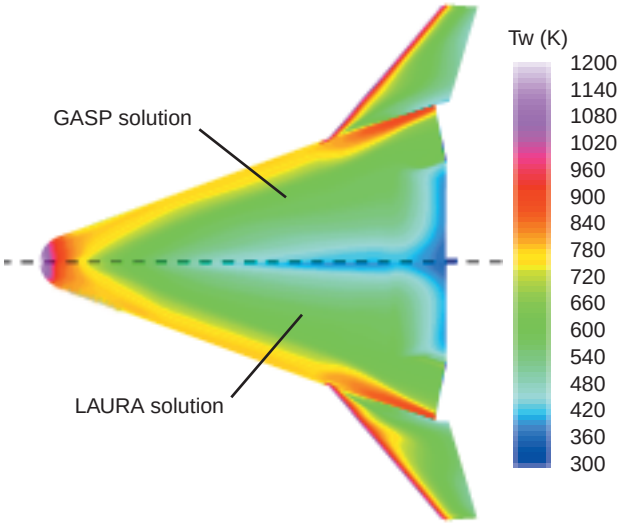

Figure 37. Computed Windward Temperatures for Case 1

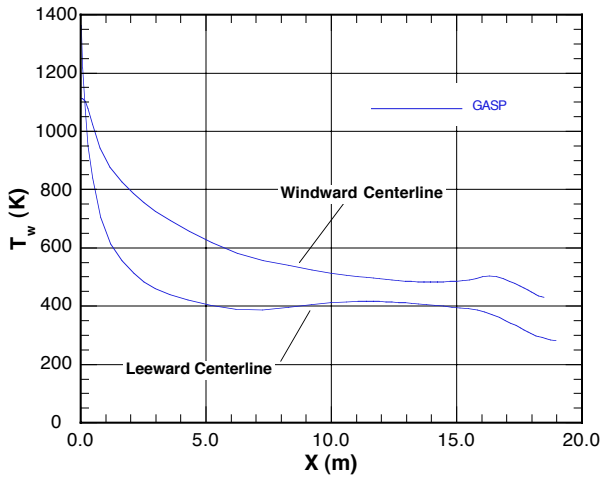

Figure 38. Computed Centerline Temperatures for Case 2

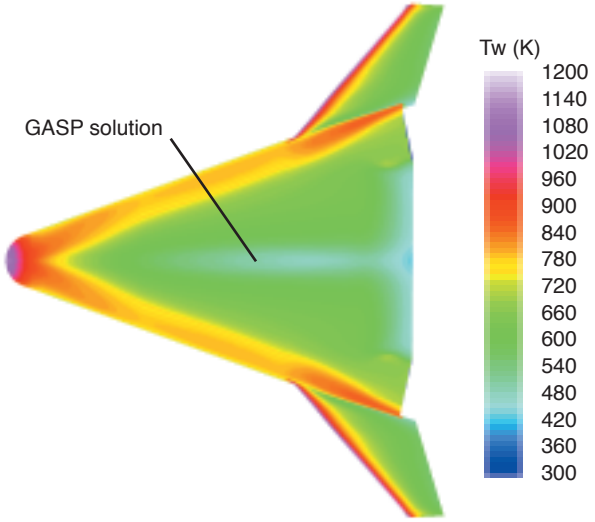

Figure 39. Computed Windward Temperatures for Case 2

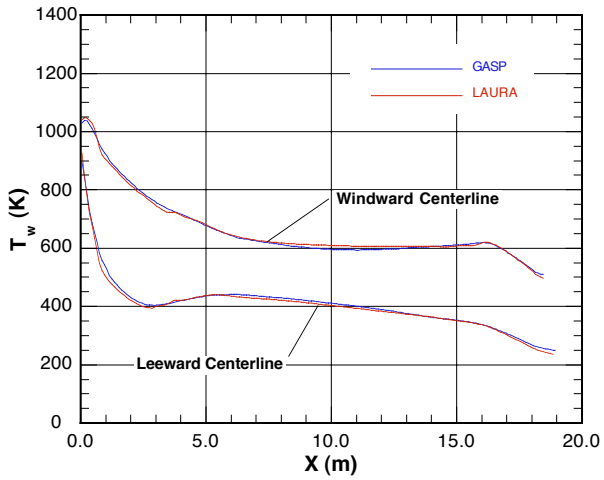

Figure 40. Computed Centerline Temperatures for Case 3

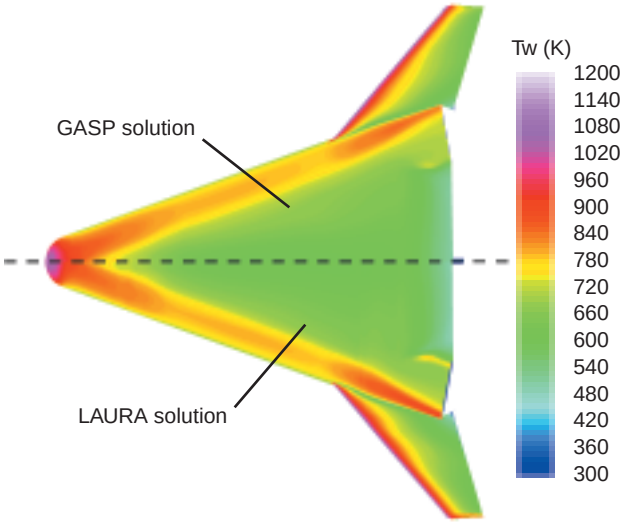

Figure 41. Computed Windward Temperatures for Case 3

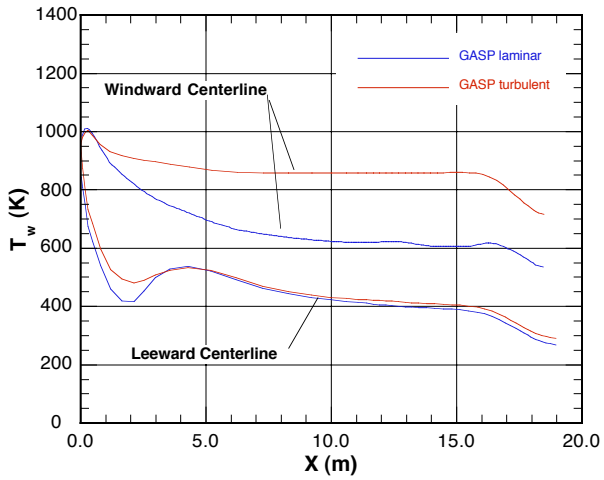

Figure 42. Computed Centerline Temperatures for Case 4

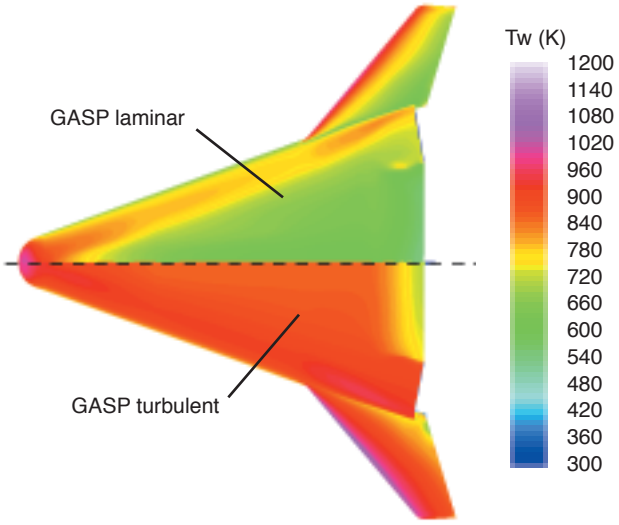

Figure 43. Computed Windward Temperatures for Case 4